Solar Energy Materials & Solar Cells 269 (2024) 112786

Contents lists available at ScienceDirect

Solar Energy Materials and Solar Cells

journal homepage: www.elsevier.com/locate/solmat

# Optimization of the mass ratio and melting temperature of PCMs integrated in Salt Gradient Solar Ponds

Daniele Colarossi [a,*], Yassmine Rghif [b]

[a] Department of Industrial Engineering and Mathematical Sciences, Università Politecnica Delle Marche, Via Brecce Bianche 12, Ancona, Italy
[b] Department of Physics, Faculty of Sciences and Techniques of Tangier, Abdelmalek Essaâdi University, Morocco

ARTICLE INFO

*Keywords:*
Mass ratio
Melting temperature
Numerical optimization
Phase change material
Salt Gradient Solar Pond
Thermal energy storage

ABSTRACT

Phase Change Materials (PCMs) are promising materials to increase the storage capacity of solar energy-based systems, such as Salt Gradient Solar Ponds (SGSPs), as they are characterized by a large latent heat during the solid-liquid phase change. This paper introduces an optimization study for PCM integration in SGSP, in terms of PCM mass ratio (14 %, 19 %, 28 % and 47 %) in the lower convective zone and PCM melting temperature (35 °C, 44 °C and 50 °C). Numerically, a 2D model is developed, consisting in the continuity equation as well on momentum, thermal energy and diffusion equations. In order to validate this numerical model, an experimental campaign of a parallelepiped SGSP with PCM capsules in the bottom is constructed. The latter is tested for two PCMs (RT35HC and RT44HC) and under different climatic conditions of March and June. Numerical and experimental have been compared in which the maximum average relative error does not exceed 4.62 %, which ensures a positive validation. The optimization returns that the final liquid fraction of PCM decreases both increasing the mass ratio and melting temperature. Higher mass ratios reduce the final temperature of the PCM (49.5 °C with 14 % and 42 °C with 47 % for RT35HC), and also with higher melting temperatures reduce the thermal energy stored, since the pond tends to work only as a sensible energy storage system.

## 1. Introduction

Renewable energies, often referred as clean energies, come from natural sources that are continually renewed [1]. Solar energy is one of these sources [2,3] It is exploited even more all over the world, where it can be harnessed to produce electricity, heat or desalinate water [4].

Salt Gradient Solar Ponds (SGSPs) are special types of collectors and solar thermal energy storage [5,6] that utilize a vertical salt stratification for the collection and storage of solar energy for various applications [7] such as seawater desalination [8,9], electricity generation [10] or some industrial applications [11,12]. It is essentially a large, shallow pool filled with water containing a controlled concentration of dissolved salts. The main principle behind a SGSP is the selective absorption and trapping of solar radiation within the pond's layers. The pond is typically divided into three distinct zones (Fig. 1), namely starting from the bottom [13–15]:

- Lower Convective Zone (LCZ): The bottom layer of the pond (Fig. 1) is the thermal energy storage region. It consists of saltwater that is highly concentrated and usually saturated with salts. This zone is also called storage zone and it is characterized by a double diffusive convection, both thermal and saline.
- Non-Convective Zone (NCZ): The middle layer of the pond (Fig. 1) is where the unique salt gradient is established [16]. It contains a controlled linear gradient of salt concentration, generally from 0 % at the top of the zone to around 26 % at the bottom. The salinity gradient acts as a natural barrier to prevent the mixing of water within the layer, due to the different densities of the solution in vertical [17].
- Upper Convective Zone (UCZ): This uppermost layer of the pond (Fig. 1) consists of pure water [18]. Its purpose is to insulate the other layers from external disturbances, such as wind and rain [19,20]. In fact, the latter may mix the layers of the NCZ and may affect its insulating property. This phenomenon may increase the heat losses and accordingly reduce the energy efficiency.

The working mechanism of a SGSP is very simple. The incident sunlight is absorbed by the base area of the pond, usually blackened, and accordingly the saltwater in the storage zone is heated by natural convection (Fig. 1). The latter consists in convective motions upward due to the difference of densities between the layers.

* Corresponding author.
*E-mail addresses:* d.colarossi@pm.univpm.it (D. Colarossi), y.rghif@uae.ac.ma (Y. Rghif).

https://doi.org/10.1016/j.solmat.2024.112786
Received 19 October 2023; Received in revised form 11 January 2024; Accepted 22 February 2024
Available online 8 March 2024

**Nomenclature**

| | |
|---|---|
| $C$ | Saline water concentration |
| $C_{P\ PMC}$ | PCM specific heat |
| $D$ | Saline water diffusion coefficient |
| $E$ | Thermal energy stored |
| $e_1$ | LCZ thickness |
| $e_2$ | NCZ thickness |
| $e_3$ | UCZ thickness |
| $f_l$ | PCM liquid fraction |
| $H$ | Total enthalpy |
| $H_{SGSP}$ | Pond height |
| I | Incident amount of solar radiation |
| $L$ | Pond width |
| $L_h$ | PCM latent heat |
| $P$ | Saline water pressure |
| $T$ | Saline water temperature |
| $T_a$ | Ambient air temperature |
| $T_{PCM}$ | PCM temperature |
| $t$ | Time |
| u,v | Velocity components |
| $x$,$z$ | Cartesian coordinates |

*Greek symbols*

| | |
|---|---|
| $\alpha$ | Saline water thermal diffusivity |
| $\beta_C$ | Concentration expansion coefficient |
| $\beta_T$ | Thermal expansion coefficient |
| $\lambda$ | Saline water thermal conductivity |
| $\lambda_{PMC}$ | PCM thermal conductivity |
| $\nu$ | Saline water kinematic viscosity |
| $\rho_{PMC}$ | PCM Density |
| $\sigma$ | Constant of Stefan-Boltzmann |
| $\varphi$ | Heat flux density |

***Subscripts***

| | |
|---|---|
| conv | Convection |
| evap | Evaporation |
| pla | Plastic |
| pol | Polyurethane |
| rad | Radiation |
| w | Saline water |

***Abbreviations***

| | |
|---|---|
| LCZ | Lower Convective Zone |
| NCZ | Non-Convective Zone |
| SGSP | Salt Gradient Solar Pond |
| UCZ | Upper Convective Zone |

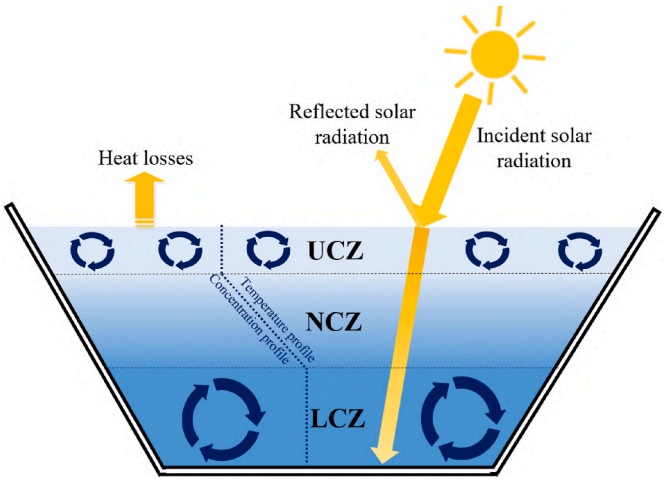


**Fig. 1.** General configuration of a SGSP [7].

This phenomenon introduces the most important limiting factor of such systems [21], namely the stability of the interface. In fact, the greater the temperature difference between the bottom of the pond and the saltwater, the greater the convective movements. This phenomenon leads the convective motions to reach the LCZ-NCZ interface, causing its fluctuation and, slowly, a reduction in the NCZ thickness. This can affect the insulating capacity of the NCZ, increasing the heat losses upward and limiting the energy efficiency of the SGSP. In case of high temperature differences in the LCZ, the strength of the convective motions can cause the rupture of the interface, which means that the heat involved in the convective motion is completely lost in the upper layers. Once the interface is damaged, the overall efficiency and durability of the pond can be compromised [22]. It is worth mentioning that, in parallel, an upward migration of the salt (and accordingly of the interface) is already present due to the difference concentration of salt in vertical, from highly concentrated on the bottom to pure water on the top [23].

One possible approach, to mitigate this limitation [7], is the incorporation of Phase Change Materials (PCMs) in the traditional configuration of SGSPs [24]. Generally, PCM refers to a category of materials that exploit the latent heat related to phase changes to store thermal energy, which usually is much larger than the sensible heat [25]. The main advantage is that the phase change theoretically occurs at a fixed temperature (or in narrow range of temperature), which means that during the phase change process the pond tends to remain at a stable and lower temperature than in a traditional pond. A reduction of temperature in the storage zone results in a more stable pond. The solution has been already investigated by different researchers. In this sense, Assari et al. [26] conducted an experimental campaign, in which two cylindrical SGSPs were constructed in Dezful, Iran. The ponds base are of 3.4 $m^2$ and depth of 1 m. The first one was a traditional SGSP, while the second one contained cylindrical capsules filled with Paraffin Wax. The experiments which were conducted in the month of July 2014, showed that the addition of PCM reduces the maximum temperature, resulting the pond more thermally stable. Ines et al. [27] conducted similar experiments but indoor under a solar simulator (both ponds with height of 22 cm and diameter of 15 cm). The test lasted 50 h, of which the lamps worked for 41 h, and during the heat extraction was noted that integrating with PCM the hot water had a more constant temperature during the process. In addition, the effect of the PCMs on the heat extraction has been investigated in another work [28]. In addition, in this case, the PCM was a paraffin wax and the heat was extracted both from the bottom of the LCZ and from the sidewalls. Results show that in the proposed solution the PCM stabilized the temperature of the outlet fluid for a longer period.

Furthermore, Rghif et al. [29] studied numerically the influence of the integration of a PCM layer to a SGSP on Dufour effect. The 2D numerical model, consisting in Navier-Stokes, heat and mass transfers equations, shows that the Dufour effect is positively affected by the integration of PCM, if the Dufour coefficient value is high and low temperature uniform heat is desirable. Colarossi et al. [30] focused, by means of the shadowgraph technique, on the integration of PCM to increase the stability of the LCZ-NCZ interface. A laboratory-scale pond was built with the sidewall in glass, and the PCM was enclosed, for the same reason, in plexiglass tubes. Both ponds, the traditional and the integrated one, were heated for 6 h, and at the end the LCZ temperature

of the PCM-integrated prototype turned out to be 3 °C less than the traditional one. What emerged through the optical analysis was that in the traditional pond the convective motions provoked a rupture of the interface, while the same phenomenon has not occurred in the integrated one, resulting the pond more stable. Assari et al. [31] studied the behaviors of two pilot ponds (with and without PCM), involving both the thermal performance and the salinity monitoring. In this work, three different heat extraction methods were investigated, and all showed that the pond with PCM reached an overall better performance (stability improved and higher outlet temperature). About the heat extraction methods, it was noted that the extraction from the NCZ has a larger influence on the stability. Therefore, the heat extraction from LCZ is more efficient.

In addition, Al-Iessa et al. [32] evaluated the impact 56 °C melting temperature PCM on a SGSP during the cold seasons. In this case, the heat released during the liquid-solid phase change is fundamental to maintain the storage temperature, increasing the overall efficiency. Two different thicknesses of PCM were used, namely 0.4 m and 0.8 m, with 21 W/m$^2$ and 25 W/m$^2$ as heat extraction rates, and the average pond efficiency increases to 11.5 % and 13.8 %, respectively. Two different melting temperatures of PCMs have been experimentally tested and compared [33]. The comparison regards a melting temperature of 35 °C and 44 °C. Higher melting temperatures smooth and reduce the maximum temperature during the day. Lower melting temperature help to stabilize the temperature during the night, as the PCM releases in the saltwater solution the latent heat. Arulprakasajothi et al. [34] conducted an experiment in South India, focusing on low solar radiation applications like the winter season. The PCM used is a paraffin wax integrated with nanoparticles of grapheme and carbon nanotubes. The aim is to increase the thermal conductivity and accordingly the heat transfer rate of the PCM. The integrated pond showed an increased the heat transfer, heat transfer coefficient, and the heat stored by 244 %, 713 %, and 83.3 %, respectively.

What emerges from a literature survey is that a standard methodology for the optimal choice of the optimal melting temperature and mass of PCM in the LCZ is still missing. The choice of these parameters is crucial as PCMs provide the maximum thermal performance in the temperature range of the phase change. With a too high melting temperature, the PCM will remain at solid state without exploiting the latent energy. On the contrary selecting a too low melting temperature the PCM will melt quickly and remain at liquid state, and it can also contribute to increase the peaks of temperature due to its lower specific heat than the saltwater solution. This paper intends to fill this gap through a numerical investigation and optimization, supported by an experimental validation, of a SGSP integrated with PCM. The aim is the optimization of the melting temperature of the PCM and the mass ratio between PCM and saltwater solution in the LCZ. To this aim, a small prototype of SGSP with PCM has been built and tested indoor under a solar simulator, which allows to reproduce the desiderate and controllable climate conditions. Then once the numerical model developed is validated, the optimization phase will return the best melting temperature and mass ratio as a function of the climate conditions.

## 2. Modeling

### 2.1. Physical model

The proposed model is a SGSP built in a parallelepiped plastic tank, of dimension 0.77 × 0.57 m$^2$ (L = 0.77 m and $H_{SGSP}$ = 0.57 m), filled according to the expected saltwater stratification, in which cylindrical tubes filled with a PCM are placed at the bottom. It is assumed as a rectangular cavity with an external layer of insulation in polyurethane (placed both on bottom and vertical walls). The thermal conductivity of the polyurethane layer is $\lambda_{pol}$ = 0.03 W/m K and its thickness is $e_{pol}$ = 0.12 m and). The PCM has been modelled as a further layer placed on the bottom, with a thickness of $e$ = 0.02 m (Fig. 2). In addition, the tank is open and serves as a seat for heat exchanges with the external environment that include radiation ($\varphi_{rad}$), convection ($\varphi_{conv}$) and evaporation ($\varphi_{evap}$).

This SGSP is composed of three layers (Fig. 2):

- Lower Convective Zone (LCZ) of thickness $e_1$ = 0.11 m. In this zone, which is located in the lowest part of the pond, there is a very high salt concentration ($C_1$ = 260 kg/m$^3$);
- Non-Convective Zone (NCZ) of thickness $e_2$ = 0.13 m. It is located above the NCZ. In this layer, the salt concentration ($C_2$) in vertical has linear pattern, decreasing while moving upwards. It acts as a thermal insulator, allowing that the energy stored can be transferred only by conduction (the saline water thermal conductivity is low) upwards;
- Upper Convective Zone (UCZ) of thickness $e_3$ = 0.03 m. This zone is relatively thin in thickness with very low in salt concentration ($C_3 \simeq$ 0 kg/m$^3$) and is located above the NCZ.

Associate this physical model with a Cartesian coordinates ($x$,$z$), in which the origin O corresponds to the bottom left corner. The $x$-coordinate is counted positively towards the right and the $z$-coordinate is computed upwards as depicted in Fig. 2.

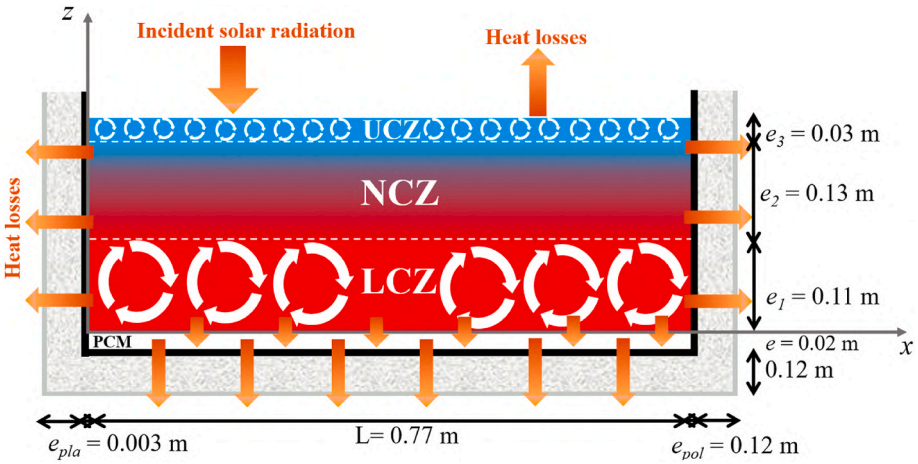


**Fig. 2.** Physical model of the considered salt gradient solar pond.

### 2.2. Mathmetical modeling

To model the transfers within the SGSP and the PCM layer, here below the assumptions made are listed:

- Salt water is assimilated to a Newtonian and incompressible fluid;
- Heat transfer is two-dimensional;
- Natural convection in the two convective zones (LCZ and UCZ) is laminar;
- Thermo-physical properties of the salt solution (water and NaCl) are constant except for the gravity term density which obeys the Boussinesq approximation;
- PCM layer is homogeneous and isotropic;
- Phase change is isothermal;
- Natural convection transfers in the liquid phase of the PCM are negligible;
- Cylindrical tubes are perfect heat conductors;
- Heat losses by radiation and convection via vertical and bottom walls of the pond are neglected.

As depicted in Fig. 2, the Cartesian coordinates ($x$,$z$) are used. Considering the above simplifying assumptions, the equations governing the transfers in LCZ and UCZ can be written as follows [35]:

- **Continuity equation**

$$\frac{\partial u}{\partial x}+\frac{\partial v}{\partial z}=0 \tag{1}$$

- **Momentum equations along [O$x$) and [O$z$) directions**

$$\frac{\partial u}{\partial t}+u\frac{\partial u}{\partial x}+v\frac{\partial u}{\partial z}=\frac{-1}{\rho}\frac{\partial P}{\partial x}+\nu\left(\frac{\partial^2 u}{\partial x^2}+\frac{\partial^2 u}{\partial z^2}\right) \tag{2}$$

$$\frac{\partial v}{\partial t}+u\frac{\partial v}{\partial x}+v\frac{\partial v}{\partial z}=\frac{-1}{\rho}\frac{\partial P}{\partial z}+\nu\left(\frac{\partial^2 v}{\partial x^2}+\frac{\partial^2 v}{\partial z^2}\right)+\left[\beta_T\,(T-\mathrm{T_i})-\beta_C(C-\mathrm{C_{min}})\right]\mathrm{g} \tag{3}$$

- **Thermal energy equation**

$$\frac{\partial T}{\partial t}+u\frac{\partial T}{\partial x}+v\frac{\partial T}{\partial z}=\alpha\left(\frac{\partial^2 T}{\partial x^2}+\frac{\partial^2 T}{\partial z^2}\right)+\frac{S}{\rho\,\mathrm{C_P}} \tag{4}$$

- **Diffusion equation**

$$\frac{\partial C}{\partial t}+u\frac{\partial C}{\partial x}+v\frac{\partial C}{\partial z}=\mathrm{D}\left(\frac{\partial^2 C}{\partial x^2}+\frac{\partial^2 C}{\partial z^2}\right) \tag{5}$$

In the NCZ, the heat transfer is by conduction and the mass transfer is by diffusion. Thus, the transfer equations in this zone:

- **Thermal energy equation**

$$\frac{\partial T}{\partial t}=\alpha\left(\frac{\partial^2 T}{\partial x^2}+\frac{\partial^2 T}{\partial z^2}\right)+\frac{S}{\rho\,\mathrm{C_P}} \tag{6}$$

- **Diffusion equation**

$$\frac{\partial C}{\partial t}=\mathrm{D}\left(\frac{\partial^2 C}{\partial x^2}+\frac{\partial^2 C}{\partial z^2}\right) \tag{7}$$

In the above equations, $u$ and $v$ are the saline water velocity components along $x$ and $z$ directions, respectively; $T$ and $C$ are the saline water temperature and saline water concentration; $\nu$ is the saline water kinematic viscosity; $\alpha$ is the saline water thermal diffusivity; $D$ is the saline water diffusion coefficient; $T_i$ and $C_{min}$ are initial temperature of the saline water and the minimum value of the saline water concentration, respectively; $\beta_T$ is the thermal expansion coefficient and $\beta_C$ is the mass expansion coefficient. In addition, the heat source term $S$ of equations (4) and (6) represents the amount of the solar radiation in input to the SGSP, which is absorbed by the saline water layers as a function of its thickness (Equation (8)).

$$S=-\frac{d\varphi_z}{dz} \tag{8}$$

With ($\varphi_z$) is calculated basing on logarithmic formula proposed by Bryant and Colbeck [36] as expressed follows:

$$\varphi_z=(1-alb)I\theta'\,(0.36-0.08\ln(z)) \tag{9}$$

With $I$ is the solar radiance amount coming to the SGSP free surface, $\theta$' is a coefficient that models the solar radiation absorption in the saline water ($\theta'=0.85$ [37]) and $alb$ is the reflected solar radiation ($alb=0.08$ [37]).

Regarding the PCM layer, the enthalpic method [38] has been used to model its thermal behavior:

$$\frac{\partial H}{\partial t}=\lambda_{\mathrm{PCM}}\left(\frac{\partial^2 T_{PCM}}{\partial x^2}+\frac{\partial^2 T_{PCM}}{\partial z^2}\right) \tag{10}$$

The total enthalpy, $H$, is equal to the sum of the sensible enthalpy ($h$ ($T_{\mathrm{PCM}}$)) and the latent enthalpy [38].

$$H=h(T_{PCM})+\rho_{\mathrm{PCM}}\,\mathrm{L_h}\,f_l \tag{11}$$

$$h(T_{PCM})=\int_{T_{PCM}}^{T_{fusion}}\rho_{\mathrm{PCM}}\,\mathrm{Cp_{PCM}}\,dT_{PCM} \tag{12}$$

With : $\lambda_{\mathrm{PCM}}$ : PCM thermal conductivity ;

$T_{PCM}$ : PCM temperature ;
$\rho_{\mathrm{PCM}}$ : PCM density ;
$\mathrm{C_{P\ PCM}}$ : PCM specific heat capacity ;
$L_h$ : PCM latent heat ;
$f_l$ : PCM liquid fraction, varying from 0 to 1 (equal to 0 at solid state and 1 at liquid state) as follows :

$$f_l=\begin{cases}0 & \text{if } T_{PCM}<\mathrm{T_{fusion}}\\ \text{if} & T_{PCM}=\mathrm{T_{fusion}}\\ 1 & \text{if } T_{PCM}>\mathrm{T_{fusion}}\end{cases} \tag{13}$$

With $\mathrm{T_{fusion}}$ is the PCM melting temperature.

Combining equations (11) and (10) gives equation (14) and subsequently equation (15).

$$\frac{\partial h}{\partial t}+\mathrm{L_h}\,\rho_{\mathrm{PCM}}\frac{\partial f_l}{\partial t}=\lambda_{\mathrm{PCM}}\left(\frac{\partial^2 T_{PCM}}{\partial x^2}+\frac{\partial^2 T_{PCM}}{\partial z^2}\right) \tag{14}$$

$$\rho_{\mathrm{PCM}}\,\mathrm{Cp_{PCM}}\frac{\partial T_{PCM}}{\partial t}=\lambda_{\mathrm{PCM}}\left(\frac{\partial^2 T_{PCM}}{\partial x^2}+\frac{\partial^2 T_{PCM}}{\partial z^2}\right)-\mathrm{L_h}\,\rho_{\mathrm{PCM}}\frac{\partial f_l}{\partial t} \tag{15}$$

For the solid ($T_{PCM}<\mathrm{T_{fusion}}$) and liquid ($T_{PCM}>\mathrm{T_{fusion}}$) states of the PCM, equation (15) is written :

$$\rho_{\mathrm{PCM}}\,\mathrm{Cp_{PCM}}\frac{\partial T_{PCM}}{\partial t}=\lambda_{\mathrm{PCM}}\left(\frac{\partial^2 T_{PCM}}{\partial x^2}+\frac{\partial^2 T_{PCM}}{\partial z^2}\right) \tag{16}$$

For $T_{PCM}=\mathrm{T_{fusion}}$, the phase change is isothermal. Therefore :

**Table 1**
*Thermo-physical proprieties of the PCMs* [39].

| | RT35HC | RT44HC | RT50HC |
|---|---|---|---|
| **PCM melting temperature (°C)** | 35 | 44 | 50 |
| **PCM density solid/liquid (kg/l)** | 0.88/0.77 | 0.8/0.7 | 0.88/0.76 |
| **PCM latent heat (kJ/kg)** | 240 | 250 | 160 |
| **PCM specific heat (kJ/kg K)** | 2 | 2 | 2 |
| **PCM thermal conductivity (W/m K)** | 0.2 | 0.2 | 0.2 |

$$\frac{\partial T_{PCM}}{\partial t} = 0 \tag{17}$$

Consequently, equation (15) is written as follows :

$$L_h\, \rho_{PCM} \frac{\partial f_l}{\partial t} = \lambda_{PCM} \left( \frac{\partial^2 T_{PCM}}{\partial x^2} + \frac{\partial^2 T_{PCM}}{\partial z^2} \right) \tag{18}$$

The above equation allows us to determine the evolution over time of the function $f_l$.

In addition, the thermo-physical proprieties of the PCMs used in this study are reported in Table 1 [39].

### 2.3. Initial and boundary conditions

- *Initial conditions*

$\forall\, t \le t_0$, where $t_0$ is initial time of the solar radiation capture by the saline solution of the SGSP, the fluid is considered at rest (u = v = 0 m/s) and at a temperature of 23.5 °C for the PCM layer and the LCZ, 19.5 °C for the UCZ and a linear variation in the NCZ. In addition, the initial NaCl concentration in the three zones is as follows:

$$\begin{cases} C(t_0,x,z) = C_1 = 260\,\mathrm{kg/m^3} & \text{with } 0 \le x \le L \text{ and } 0 \le z \le e_1 \\ C(t_0,x,z) = C_2 = (480 - 2000\,z)\,\mathrm{kg/m^3} & \text{with } 0 \le x \le L \text{ and } e_1 \le z \le e_1 + e_2 \\ C(t_0,x,z) = C_3 = 0\,\mathrm{kg/m^3} & \text{with } 0 \le x \le L \text{ and } e_1 + e_2 \le z \le H_{SGSP} \end{cases} \tag{19}$$

- *Boundary conditions*

$\forall\, t > t_0$, both velocity components are considered null at the free surface, at the bottom and vertical walls of the SGSP as shown in (20).

$$\begin{cases} u(t,x,z) = v(t,x,z) = 0\ \mathrm{m/s} \text{ with } 0 < z < H_{SGSP} \text{ and } x = 0 \text{ or } x = L \\ u(t,x,z) = v(t,x,z) = 0\ \mathrm{m/s} \text{ with } z = 0 \text{ and } 0 < x < L \\ v(t,x,z) = v(t,x,z) = 0\ \mathrm{m/s} \text{ with } z = H_{SGSP} \text{ and } 0 < x < L \end{cases} \tag{20}$$

Moreover, the vertical and bottom walls are in polymeric material ($e_{pla} = 0.003$ m and $\lambda_{pla} = 0.4$ W/m K) and insulated with polyurethane ($e_{pol} = 0.12$ m and $\lambda_{pol} = 0.12$ W/m K). The boundary conditions imposed on the temperature and salt concentration are as follows:

- At the left ($x = 0$ and $0 < z < H_{SGSP}$) and right ($x = L$ and $0 < z < H_{SGSP}$) pond walls :

$$\lambda \frac{\partial T}{\partial x} = -\frac{Tw_{in} - T_a}{\frac{e_{pla}}{\lambda_{pla}} + \frac{e_{pol}}{\lambda_{pol}}} \; ; \; \frac{\partial C}{\partial x} = 0 \tag{21}$$

- At the SGSP surface ($z = H_{SGSP}$ and $0 < x < L$) :

$$\lambda \frac{\partial T}{\partial z} = -\varphi_{tt} \; ; \; \frac{\partial C}{\partial z} = 0 \tag{22}$$

- At the PCM-bottom interface ($z = 0$ and $0 < x < L$) :

$$\lambda \frac{\partial T}{\partial z} = \lambda_{PCM} \frac{\partial T_{PCM}}{\partial z} ; \; \frac{\partial C}{\partial z} = 0 \tag{23}$$

- At the left ($x = 0$ and -e $< z < 0$) and right ($x = L$ and -e $< z < 0$) walls of the PCM :

$$\lambda_{PCM} \frac{\partial T_{PCM}}{\partial x} = -\frac{Tw_{in} - T_a}{\frac{e_{pla}}{\lambda_{pla}} + \frac{e_{pol}}{\lambda_{pol}}} \tag{24}$$

- At the PCM bottom ($z =$ -e and $0 < x < L$) :

$$\lambda_{PCM} \frac{\partial T_{PCM}}{\partial z} = -\frac{Tw_{in} - T_a}{\frac{e_{pla}}{\lambda_{pla}} + \frac{e_{pol}}{\lambda_{pol}}} \tag{25}$$

With $T_{Win}$ is the temperature at the wall inner face and $\varphi_{tt}$ of (22) represents the density flux exchanged between the water surface of the SGSP and its surrounding environment according to the following balance:

$$\varphi_{tt} = \varphi_{conv} + \varphi_{evap} + \varphi_{rad} \tag{26}$$

More calculation details of these densties are reported in our previous work [23].

### 2.4. Numerical methodology

Equations are solved numerically basing on the Finite Volume Method (FVM) and FORTRAN 95 programming language. The temporal and spatial discretizations are performed using the implicit method and central schema, respectively. The Semi-Implicit Method for Pressure-Linked Equations (SIMPLE algorithm) [40] is employed for Navier-Stokes equations. Then, the Gauss method is applied to dissolve the resulting algebraic system. To accelerate the convergence, under relaxation factors are used (0.5 for the temperature and salt concentration and 0.8 for the velocity [40]). The calculations are conducted until the following convergence criterion is achieved:

$$\left| \frac{\Phi^{t+\Delta t} - \Phi^{t}}{\Phi^{t+\Delta t}} \right| \le 10^{-8} \text{ where } \Phi = (u, v, T, C) \tag{27}$$

Fig. 3 illustrates the flow chart of the numerical model developed.

## 3. Materials and measurement system materials-methods

### 3.1. Solar pond description

The experimental tests were used as validation for the numerical model proposed. Tests were performed under a solar simulator [41], in order to set and control the desired climatic conditions and also to avoid the fluctuation of the natural outdoor conditions. It should be noted that the design and validation phases of the solar simulator were widely discussed in a previous work [41]. It is worth mentioning that the validation procedure followed the international standard "IEC 60904–9:2020 - Photovoltaic devices - Part 9: Classification of solar simulator characteristics". This ensured the quality of the artificial light regarding the stability of the luminous flux in time and the uniformity over the target area, which was approximately around 2 m × 1 m. In addition, the lamp array could vary its distance (by means of a vertical guide) with the target area to adjust the intensity of the artificial solar radiation. This way the intensity could be increased or decreased to simulate the typical daytime profile. Fig. 4 shows the experimental prototype, built according to the dimensions used in the numerical phase.

Generally, Phase Change Materials can be divided in three different

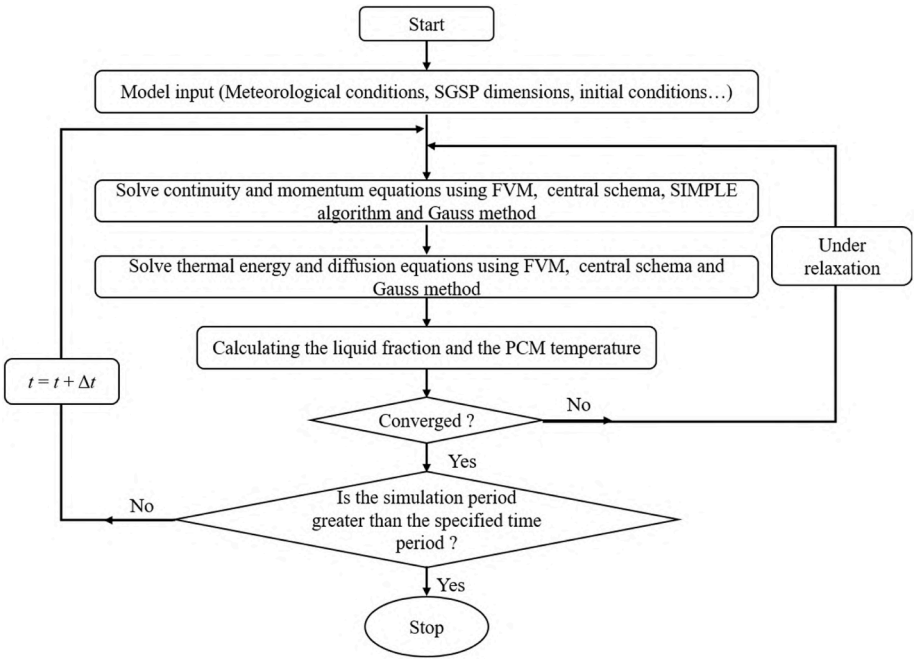


**Fig. 3.** Flow chart of the numerical model developed.

categories: organic (paraffin and fatty acids), inorganic (salt hydrates and metallic) or eutectic [38]. The selected PCM for this work was a paraffin wax, which belongs to the first group. The advantages of this category of PCMs are the good compatibility with other materials, the recyclable, the absence of supercooling, the high heat of fusion and the availability in a large range of temperatures. The disadvantages are the flammability, the low thermal conductivity and the relatively large volume change during the solid-liquid phase change. The PCMs were purchased from Rubitherm (Germany), and are called RT35 HC and RT44 HC, which means that they have a melting temperature of 35 °C and 44 °C, respectively. The PCM, aiming to increase the storage capacity and the stability of the pond, was added in the LCZ laid on the bottom. The PCM was contained in 0.6 m length tubes made of galvanized steel. They all had an internal and external diameter of 0.042 m and 0.049 m, and were placed parallelly to each other (Fig. 5).

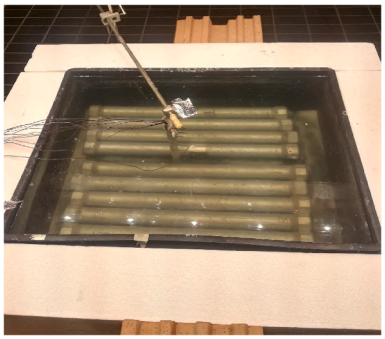

**Fig. 5.** Arrangement of the PCM in the pond.

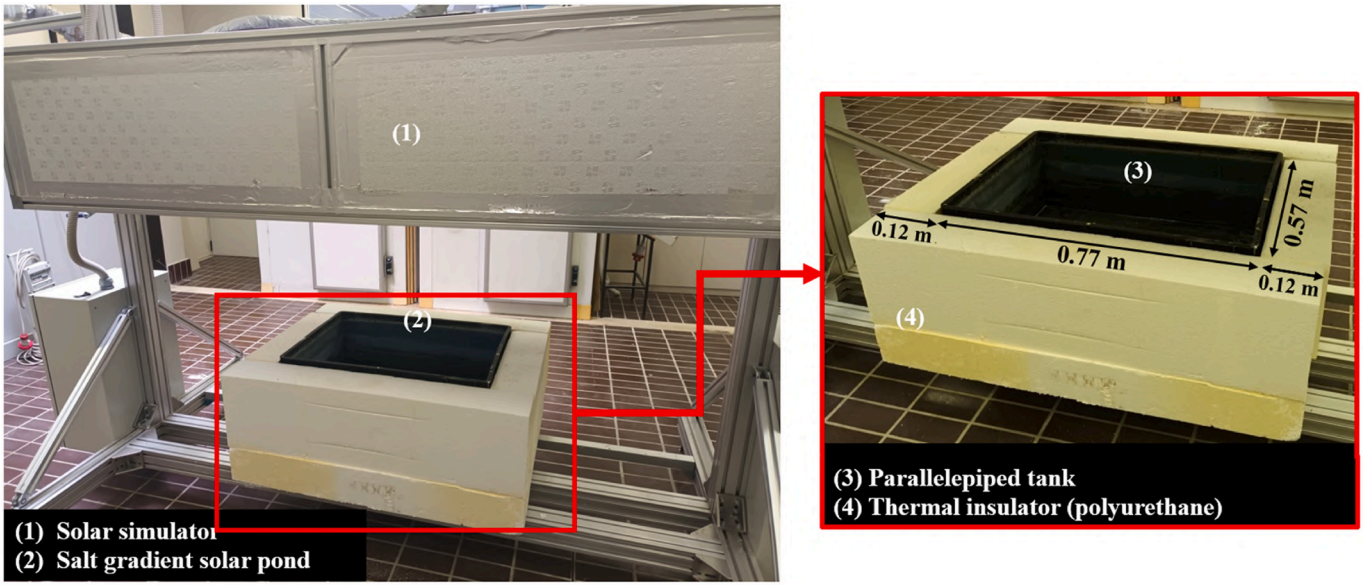


**Fig. 4.** Prototype of the built pond.

Considering the 12 % of volumetric expansion passing from solid to liquid, the paraffin wax was first melted and poured liquid into the tubes. This ensured that the maximum volume occupied by the PCM did not exceed the volume of the tube, in fact during the solidification phase there is a reduction of the volume. The other properties of the galvanized steel were the density, 7800 kg/m3, the thermal conductivity, 55 W/m K, and the specific heat capacity, 502 J/kg K.

### 3.2. Measurement system

Regarding the measurement systems, temperatures, relative humidity and solar radiation were monitored. T-type thermocouples (±1.0 °C accuracy) were used to monitor the distribution vertical of the temperatures in of the salt water (Fig. 6). These thermocouples were placed in a transparent vertical tubes located at the center of the pond section. This way the boundary effects were limited. The arrangment of the thermocouples was the following:

- Three in the LCZ placed at 0 m, 0.06 m and 0.11 m from the bottom (Fig. 6);
- Four in the NCZ at 0.15 m, 0.18 m, 0.21 m, and 0.24 m from the bottom (Fig. 6);
- One in the UCZ at 0.27 m from the bottom (Fig. 6).

The data acquisition chain consisted of data logger connected to a software for data visualization. Regarding the solar radiation, the pyranometer model DPA/ESR 154, was used to monitor. The main characteristics of this sensor was the range of measure, from 0 to 2000 W/m2, a sensitivity of 10.88 μV/W m−2, and a linearity of 0.75%. The environmental conditions were measured by means of the Omega HX93BD, which allowed to monitor the relative humidity and the air temperature (placed close to the pond). The ranges of measure and the accuracies were from −30 °C to 75 °C and ±0.6 °C for the temperature sensor, while from 0 % to 100 % and of ±2.5 % for the relative humidity one.

**Table 2**
Range measure and uncertainty of the measurements system.

| | Measured property | Range measure | Uncertainty |
|---|---|---|---|
| T-type thermocouples rowhead | Saltwater temperature | From −250 °C to 400 °C | ±1.0 °C |
| Pyranometer model DPA/ESR 154 rowhead | Solar radiation | From 0 to 2000 W/m2 | <5 % |
| Omega HX93BD rowhead | Relative humidity | From 0 % to 100 % | ±2.5 % |
| Omega HX93BD rowhead | Air temperature | From −30 °C to 75 °C | ±0.6 °C |

Table 2 sumurizes the range measure as well as the uncertainty of the measurements system.

## 4. Results and discussion results

### 4.1. Numerical model validation: comparisons between numerical and experimental results

This part aims to compare numerical and experimental results and therefore the validation of the numerical model. Then, the latter will be used to optimize the melting temperature of the PCM and the mass ratio in the LCZ. For a better completeness, the validation procedure is proposed for four different experimental conditions, varying both the climatic conditions reproduced (March and June) and the melting temperature of the PCM (35 °C and 44 °C). Each tests lasted 72 h and have been performed reproducing the daily average solar radiation profile of Ancona (Italy):

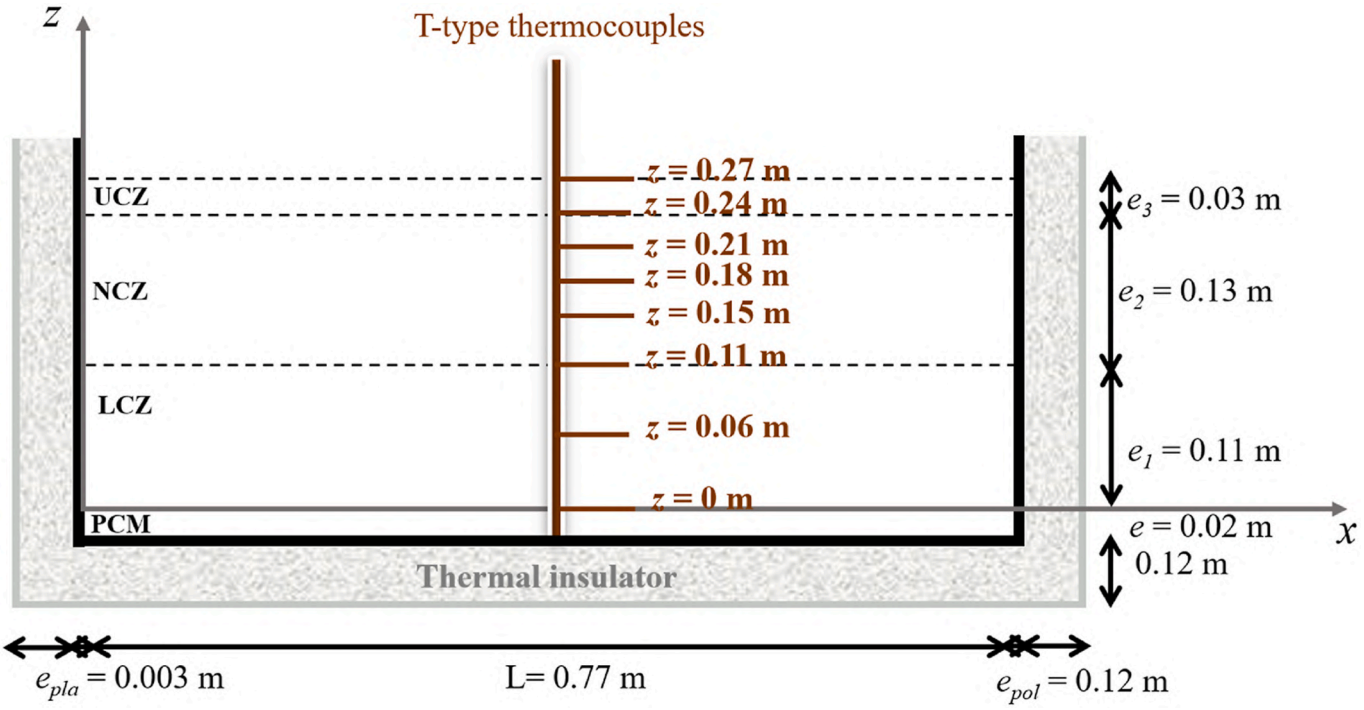


**Fig. 6.** Schematic diagram of the arrangement of temperature measurement points.

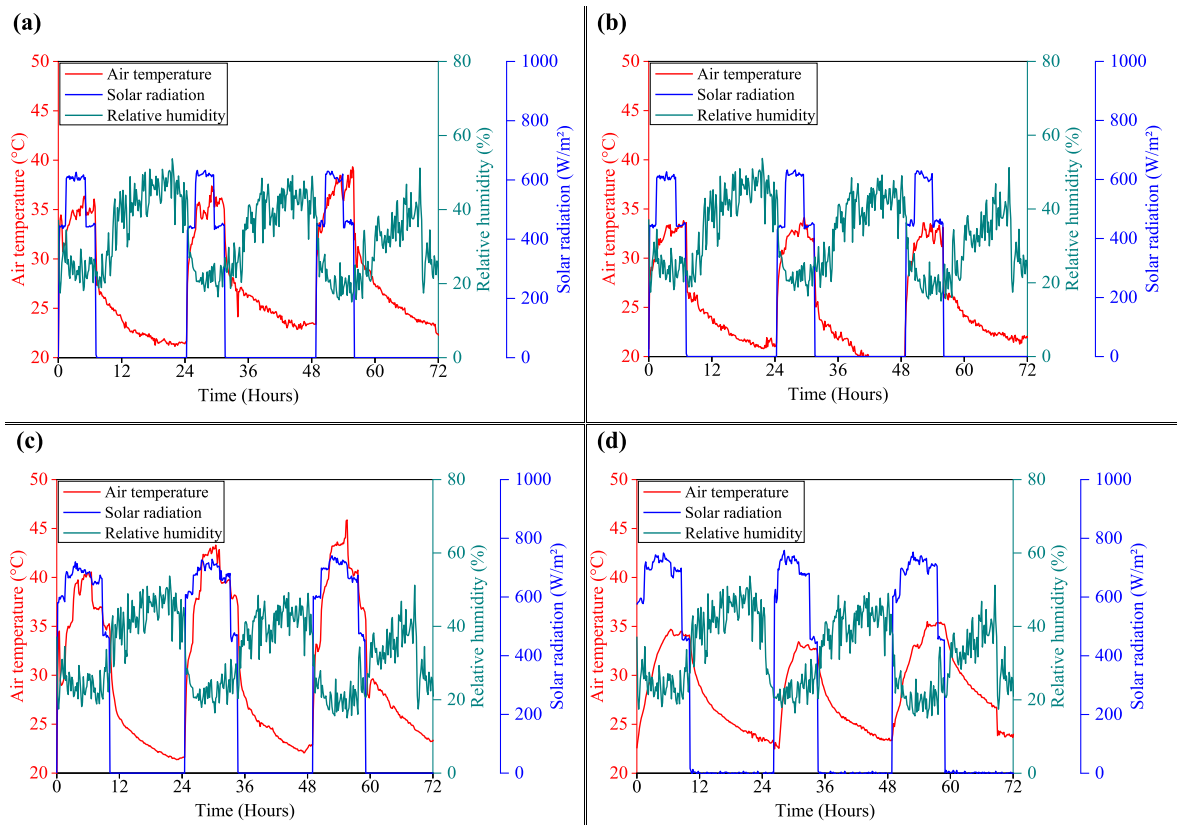


**Fig. 7.** Measured data of (a) case 1, (b) case 2, (c) case 3 and (d) case 4.

- Case 1: the PCM chosen is the RT35HC (melting temperature of 35 °C) tested under the climatic conditions of a typical day of March;
- Case 2: the PCM chosen is the RT44HC (melting temperature of 44 °C) tested under the climatic conditions of a typical day of March;
- Case 3: the PCM chosen is the RT35HC (melting temperature of 35 °C) tested under the climatic conditions of a typical day of June;
- Case 4: the PCM chosen is the RT44HC (melting temperature of 44 °C) tested under the climatic conditions of a typical day of June.

Fig. 7 illustrates the measured data (air temperature Ta, solar radiation I and relative humidity Hr) of each case considered. It should be noted that the values on the x-axis of all results figures correspond to the duration of the test (72 h), and the beginning was at 9:00.

The comparison regards the temporal evolution of the average temperatures in the PCM layer (Fig. 8) as well as in the LCZ, UCZ and NCZ (Fig. 9). The two different climatic conditions (March and June) have been chosen to better prove the validity of the numerical model proposed. In fact, during the summer season (June) the melting process of the PCM is complete and the temperatures reached exceed the melting one (Fig. 8-c and 8-dFig. 8-). In the intermediate month (Fig. 8-a and 8-b), only the RT 35HC reaches the melting temperature during the second and the third day of the experimental phase (Fig. 8-a). The proposed scenarios allow to reproduce most of the conditions that a SGSP can encounter.

Fig. 8 shows the temporal evolution of the temperatures in the PCM layer obtained numerically and measured experimentally. The values on the x-axis correspond to the duration of the test, and the beginning was at 9:00. As it can be seen, the experimental and numerical results show a good agreement in which the average relative error is 2.84 % for case 1, 3.01 % for case 2, 3.70 % for case 3 and 1.40 % for case 4.

Fig. 9 shows the comparison between numerical and experimental average temperatures of LCZ, NCZ and UCZ versus time. The values on the x-axis correspond to the duration of the test, and the beginning was at 9:00. Due to the salt concentration stratification, the absorbed solar energy is trapped on the SGSP bottom and therefore the LCZ temperature increases by natural convection. In fact, the average temperature of LCZ is higher than that of NCZ and UCZ, especially in summer season in which the intensity of the solar radiation is highest (Fig. 9-d). Overall, the maximum recorded value (about 51 °C numerically and 53 °C experimentally) is for LCZ in case 4 (Fig. 9-d). Moreover, a good agreement between numerical and experimental UCZ, NCZ and UCZ temperatures during the 72 h is observed. The maximum errors are measured in the diurnal peaks of temperatures of the LCZ, as there is the maximum heat absorption of the solar radiation from the bottom of the pond, which directly influences the temperature of the LCZ.

To prove the good accuracy and confidence of the numerical model, the average relative error is calculated for each case considered. Table 3 summarizes the average relative errors obtained. The maximum error corresponds to 4.33 %, which means that all the cases show a less that 5 % error. Accordingly, the numerical model proposed can be considered accurate.

### 4.2. *Numerical optimization of mass ratio and melting temperature*

The parameters chosen for the optimization are the melting temperature of the PCM and the mass ratio in the LCZ. The melting temperatures simulated are 35 °C, 44 °C and 50 °C, while the mass ratios are 14 %, 19 %, 28 % and 47 %. It should be noted that the thermophysical proprities of the PCMs are reported in Table 1. Moreover, the initial temperature of the saline water is considered homegenous in all the pond and equal to 30 °C for RT35HC and 40 °C for RT44HC and RT50HC.

As mentionned in the last paragraph of introdution, the main aim of this study is to chose the PCM that maximaze the SGSP perfomance. The optimal melting temperature of PCM will be the one that works most of the time in the melting temperature range. In fact, in this range, the PCM

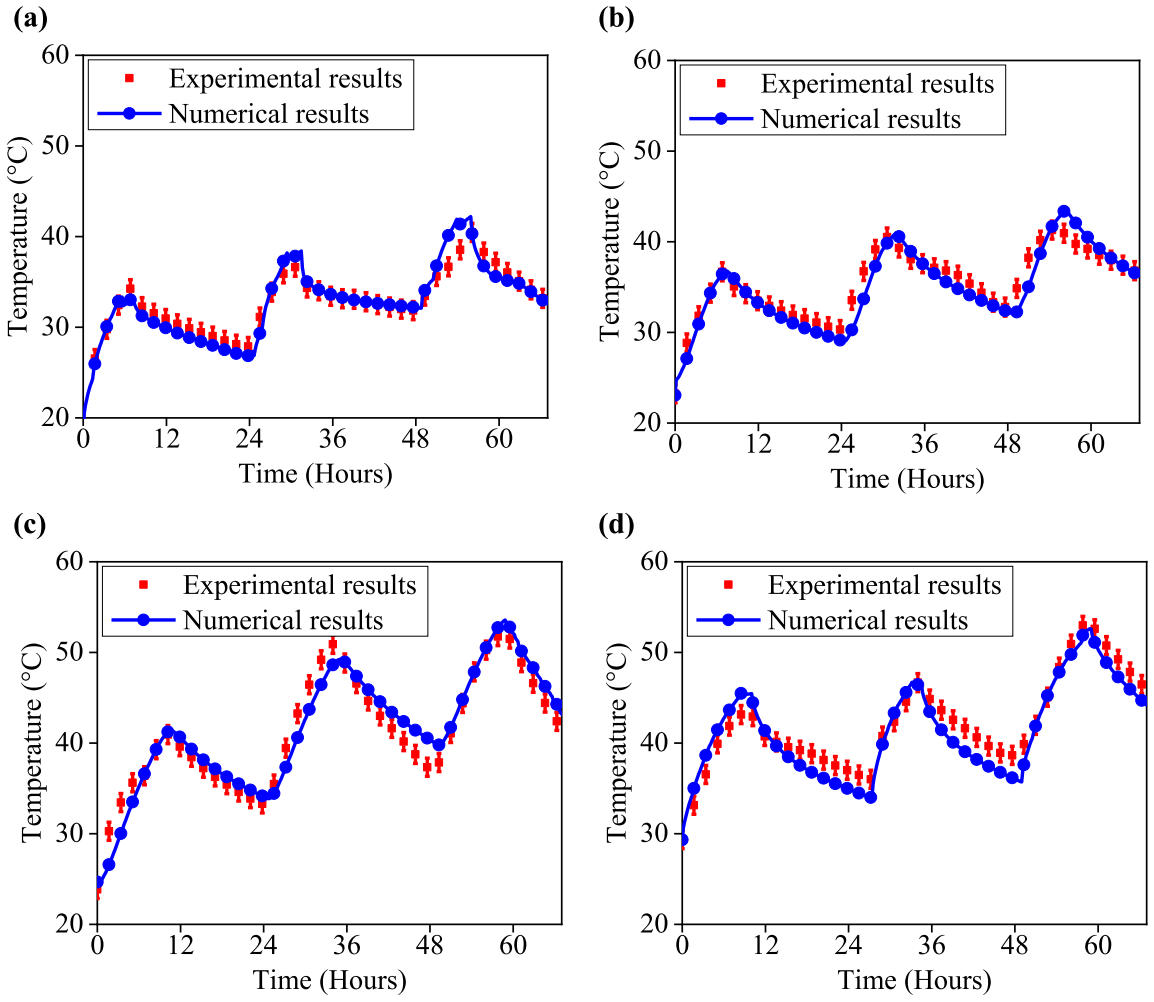


**Fig. 8.** Temperature variation of the PCMs for (a) case 1, (b) case 2, (c) case 3 and (d) case 4.

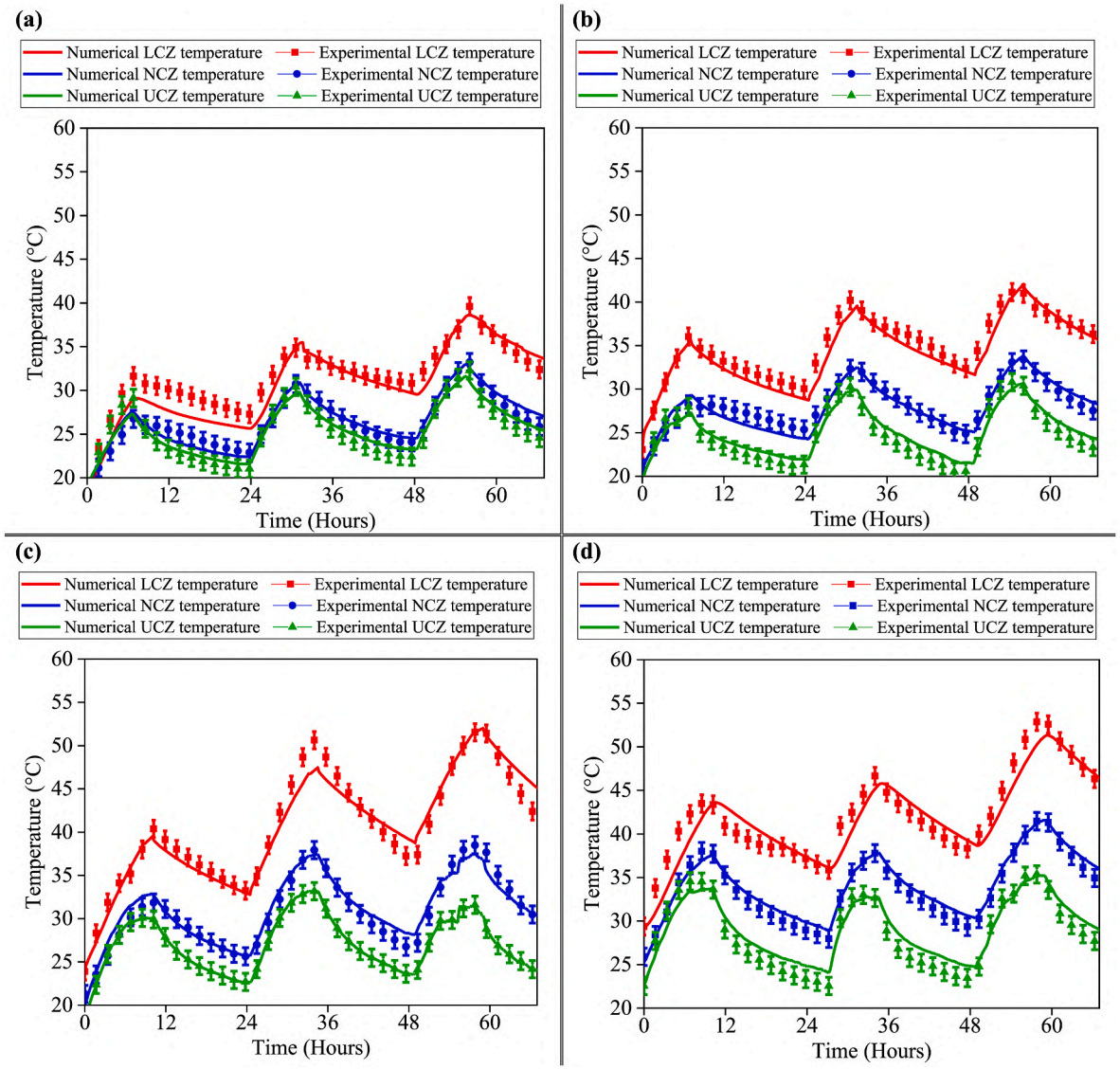


**Fig. 9.** Numerical and experimental temperature variation of LCZ, NCZ and UCZ for (a) case 1, (b) case 2, (c) case 3 and (d) case 4.

**Table 3**
Average relative error for each case considered.

| | Average relative error (%) | | | |
|---|---|---|---|---|
| | PCM layer | LCZ | NCZ | UCZ |
| Case 1: RT35HC and March rowhead | 2.84 | 4.33 | 2.35 | 2.84 |
| Case 2: RT44HC and March rowhead | 3.01 | 2.54 | 2.48 | 3.78 |
| Case 3: RT35HC and June rowhead | 3.70 | 2.84 | 2.51 | 4.62 |
| Case 4: RT44HC and June rowhead | 1.40 | 1.45 | 0.57 | 1.05 |

contributes more to stabilizing the pond temperature, and therefore increasing its thermal capacity. This is due to its high latent heat, which allows to store large amount of thermal energy at a nearly constant temperature. Regaridng the second parameter, the optimal mass ratio is the one that allows to the PCM to fully melt during the period of interest. In case of a too high mass of PCM, the majority of it will remain at the solid state and will also act as a thermal insulator (considering its thermal conductivity equal to around 0.2 W/m k). On the contrary, a too low mass of PCM will quickly melt and then will contribute to overheat the pond, due to its lower specific heat compared to that of the saltwater solution.

#### 4.2.1. *Temperature and liquid fraction variations of the PCM layer*

Figs. 10–12 illustrate the temporal evolution of the temperatures and liquid fraction in the PCM layer at the different mass ratios, for a melting temperature of 35 °C, 44 °C and 50 °C, respectively. The temperatures are plotted with continuous lines and refer to the right-side axes, while the liquid fractions with dotted lines, referring to the left-side axes. Results are shown for three different points of measurement, called upper, middle and bottom. The upper point refers to the interface between PCM and saltwater solution of the LCZ and provides the information about the beginning of the phase changes in the PCM. The bottom point refers to the interface between the PCM and the bottom of the pond, and it is interesting to highlight the end of the phase change processes. The middle point represents the average behavior of the overall PCM layer.

Results show that there are generally three periods (Figs. 10–12). The first is the solid phase, in which the temperature of the PCMs is lower than its melting temperatures (35 °C for RT35HC, 44 °C for RT44HC and 50 °C for RT50HC) and the liquid fraction value is equal to zero. The second is the phase change, in which the PCM temperature is almost constant (theoretically an isothermal change), equal to its melting temperature, and the paraffin waxes absorb heat and store it as latent heat. During this phase, the liquid fraction starts from 0 with solid

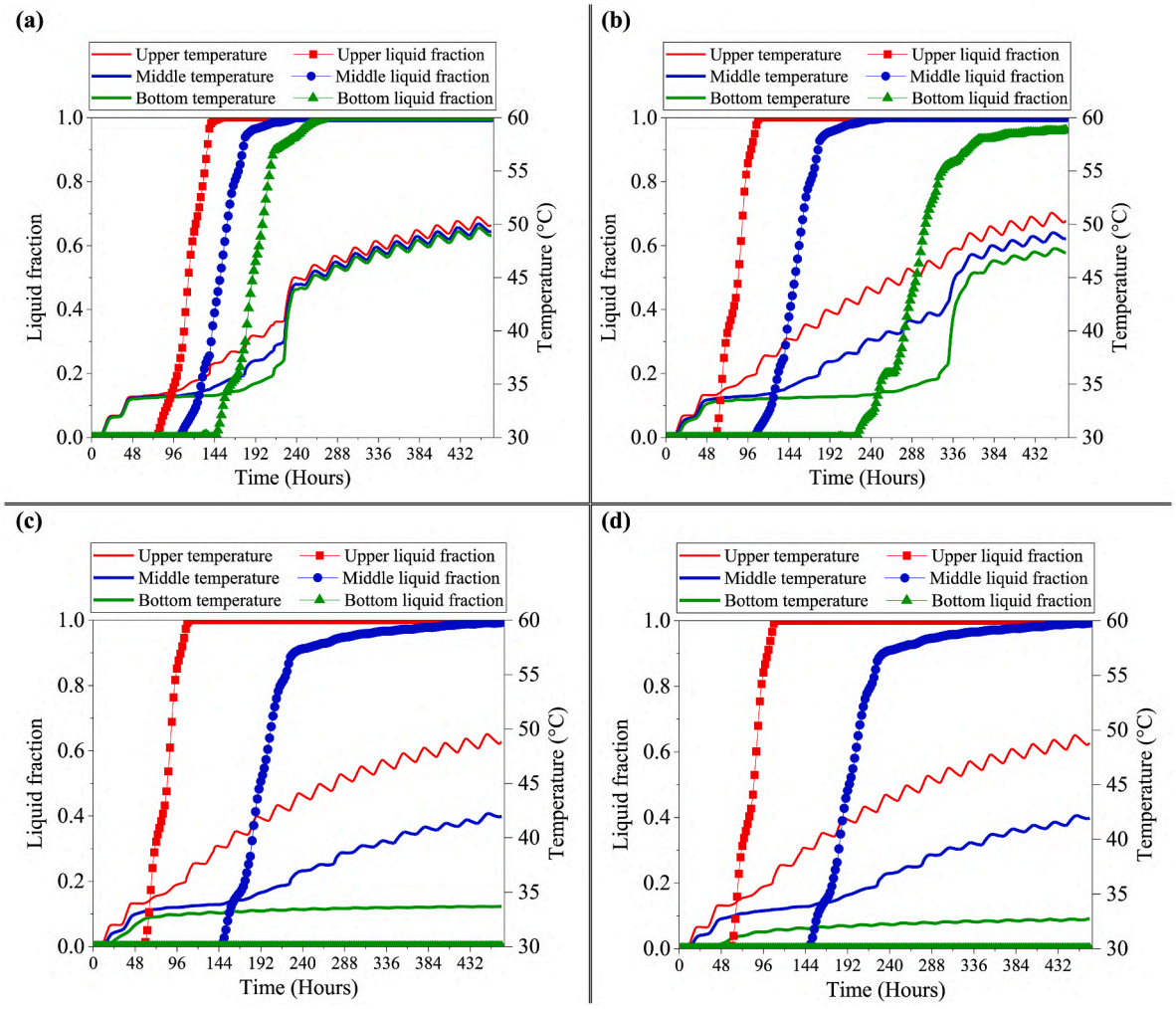


**Fig. 10.** Temperature and liquid fraction variations of RT35HC for a mass ratio of (a) 14%, (b) 19%, (c) 28% and (d) 47%.

PCM and up to 1 at the end of the melting process. The third one is the liquid phase, with a increase sinusoidal of the PCM temperature due to the variation in solar radiation during the day/night cycles. These three phases are the result of the enrgy suply by the SGSP storage zone (LCZ). In addition, it can be seen that the melting process of the upper part of the PCM is faster. This is manly due to the direct contact between the PCM and LCZ, where heat transfer is higher.

According to Figs. 10–12, the complete process is never reached for mass ratios equal to 28 % and 47 %, regardless of the melting temperature. Except for the RT35HC (Fig. 10-c and 10-dFig. 10-), in which the average point works for half time above the 90 % of liquid fraction. For the other cases, the melting process is completed for the RT35HC case with the 14 % (Fig. 10-a) at the half of the period analyzed and with the 19 % (Fig. 10-b), where the bottom layer of the PCM completes the process almost at the end of the period. As regard the RT44HC cases, the ones with 14 % (Fig. 11-a) and 19 % (Fig. 11-b) are characterized by the end of the process, for the middle point, around the end of the analysis period. This can be considered the optimal conditions, even if the bottom layer of the PCM does not reach the liquid phase, as the middle layer is representative of the overall layer. In the RT50HC cases, the PCM is always at the solid state, proving that the melting temperature is too high for the pond and the climatic conditions studied.

### 4.2.2. *Average variation of the PCM and LCZ temperature*

Another important evaluation in the selection of the optimal case is the energy stored during the entire period. In fact, the previous paragraph can give information about the effectiveness of the exploitation of the PCM, but not about the overall efficiency. On the contrary, the energy stored allows to evaluate the possible thermal output from the solar pond.

The thermal energy stored is calculated both for saltwater solution and for the PCM layer. Regarding the saline solution, the energy stored (Esto) can be calculated with the following equation as it is a sensible heat storage:

$$E_{sto} = \rho\, Cp \iint \left(T_f - T_i\right)\, dx\, dz \tag{27a}$$

Where $E_{sto}$ is the energy store, $\rho$ and $Cp$ are the density and the specific heat of the saline solution, respectively. $T_f$ and $T_i$ are the final and initial temperature of the saline solution, respectively.

For the PCM layer, Equation (27) can be used at solid and liquid phases by replacing $\rho$ by $\rho_{PCM}$, $C_P$ by $C_{p\ \mathrm{PCM}}$ and saline water temperatures by PCM temperatures. For the phase change process, the thermal energy stored ($E_{PCM}$) is a function of the liquid fraction of the PCM (latent heat storage) as represents the following equation:

$$E_{PCM} = m_{PCM}\, f_l\, T_{PCM} \tag{28}$$

Where $m_{PCM}$ is the mass of the PCM layer, $f_l$ and $T_{PCM}$ are the liquid fraction and the temperature of the PCM layer.

Fig. 13 illustrates the variation of the thermal energy stored by the proposed system for different values of mass ratio (14 %, 19 %, 28 % and 47 %) and PCMs examined in this study (RT35HC, RT44HC and

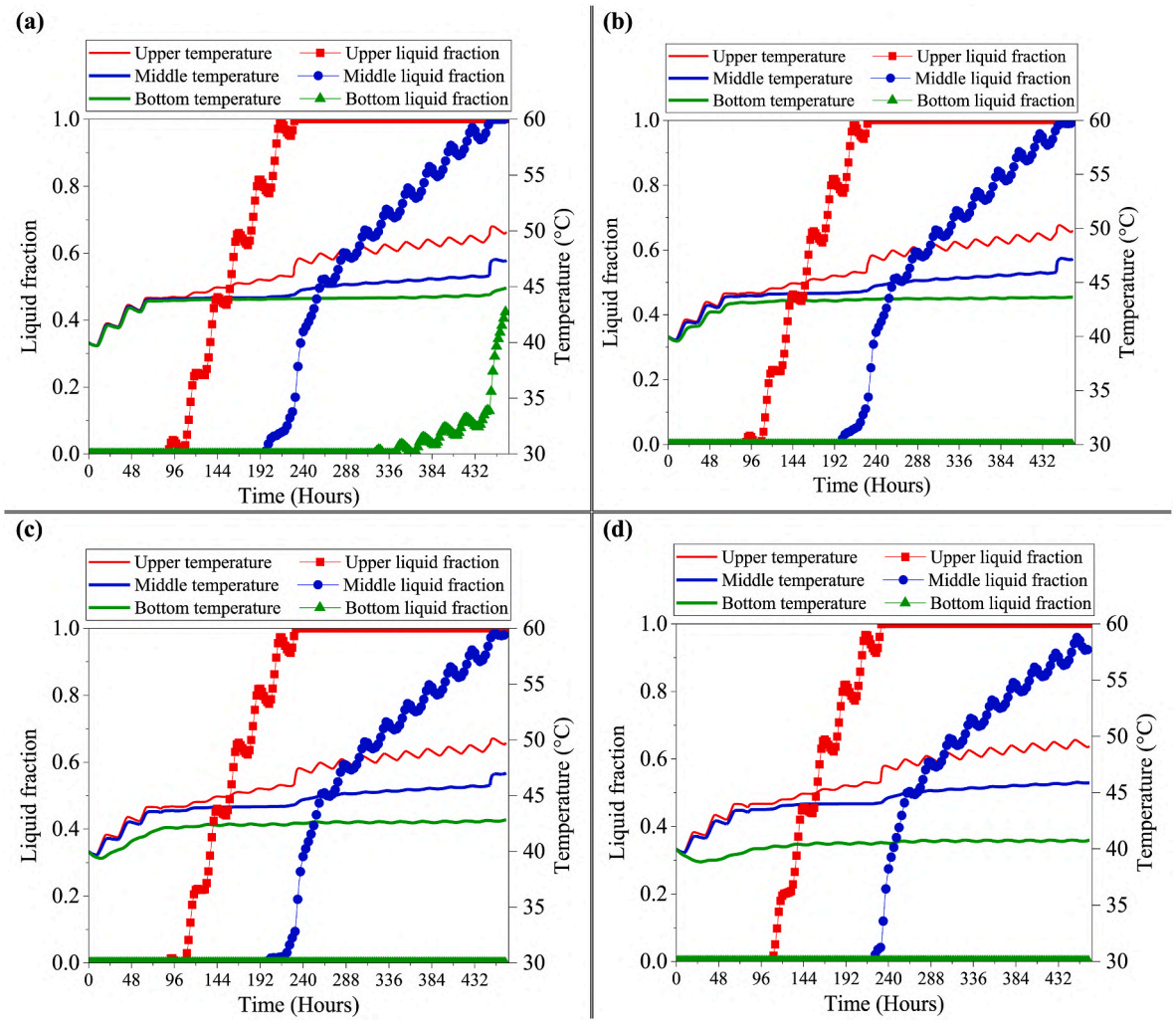


**Fig. 11.** Temperature and liquid fraction variations of RT44HC for a mass ratio of (a) 14%, (b) 19%, (c) 28% and (d) 47%.

RT50HC). What emerges from the results is that all the RT50HC cases, regardless for the mass ratio of PCM, show a drop in the energy stored compared to the RT35HC and RT44HC cases. For example, for a mass ratio equal to 47 %, it is about 8154.69 kJ for RT35HC and about 3898.32 kJ for RT50HC (a difference of 4256.37 kJ). This is due to the lack of exploitation of the latent heat of the PCM. In those, the PCM works only as at solid state, storing accordingly only sensible heat. On the contrary for the other two PCMs (RT35HC and RT44HC), the phase change is fully or almost fully complete and this returns a higher energy storage due to the latent heat contribution. Regarding the mass ratios, results are quite similar especially for RT35HC and RT44HC. As shown in the previous paragraph, a lower mass ratio will shorten the time necessary to complete the melting process. Therefore, a decrease of the amount of the latent heat stored by the PCM. This could be useful in case of multiple heat extractions during the analyzed period, in order to exploit several times the process and the consequent stabilization of the temperature in the LCZ, which increases the stability of the LCZ/NCZ interface.

## 5. Conclusions

This paper presents an optimization of the mass ratio and melting temperature of phase change materials integrated in salt gradient solar pond. The performance of the latter in fact, can be improved by PCMs, regarding both the thermal energy storage capacity and the stability of the interface, one of the main limiting factors of SGSPs. In this sense, a numerical model was developed. The latter includes the continuity, momentum, thermal energy and diffusion equations. The model was tested and validated with an experimental campaign. To this aim, a parallelepiped SGSP was constructed and integrated with PCM, encapsulated and placed on the bottom of the LCZ. For a better completeness, different cases were tested, namely two PCMs (RT35HC and RT44HC) and two different climatic conditions reproduced under a solar simulator. The comparison returned a maximum average relative error of 4.62 %, proving that the numerical model proposed is well validated. In the optimization phase, four different PCM mass ratios were simulated (14 %, 19 %, 28 % and 47 %) and three PCMs (RT35HC, RT44HC and RT50HC) with different melting temperatures (35 °C, 44 °C and 50 °C). The main findings of this study can be listed as follows:

- Increasing the melting temperature, with equal mass ratio, reduces the liquid fraction of PCM at the end of the studied period. Averagely, the RT35HC shows a quick complete melting process, while the RT50HC remains at solid state.
- Increasing the mass ratio of the PCM, with equal melting temperature, reduces the liquid fraction. This is due to the increase of the latent heat available in the pond, which requires larger inlet energy to fully melt. The correlation is less visible than melting temperature.
- Both increasing the melting temperature and the mass ratio, the final PCM temperature is lower. This can increase the stability of the pond, as lower and more stable temperatures reduce the convective motions.

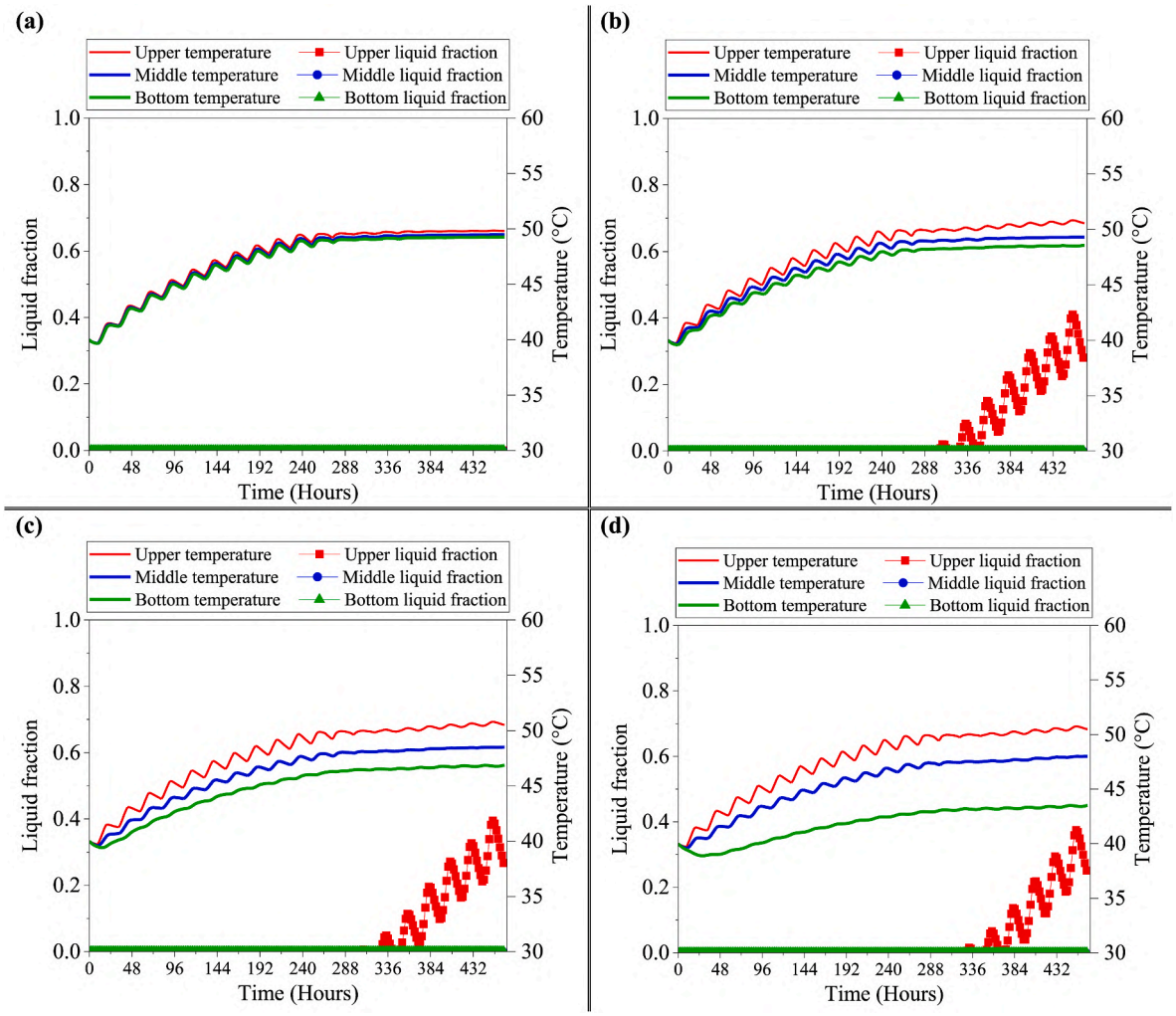


**Fig. 12.** Temperature and liquid fraction variations of RT50HC for a mass ratio of (a) 14%, (b) 19%, (c) 28% and (d) 47%.

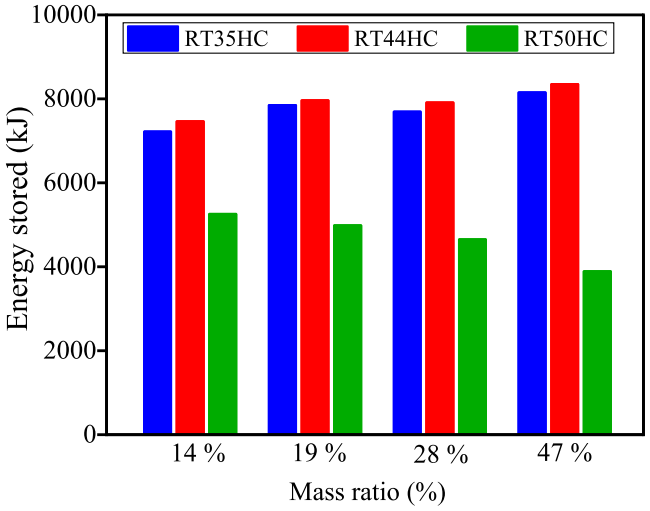


**Fig. 13.** Energy stored for each case analyzed.

- The last evaluation shows that with a too high melting temperature (in this case 50 °C) the energy stored drops. In this case, the LCZ works only as a sensible energy storage system, which can only increase its temperature and accordingly the heat losses. In addition, the solid PCM tends to work as a thermal insulator.

Future research may focus on the heat extraction phase of the thermal energy stored, investigating how the outlet temperature of the fluid is affected by the presence of PCM (basing on exergy and stratification analyses). In addition, the proposed system may be studied under longer period of time and under different climatic conditions.

## CRediT authorship contribution statement

**Daniele Colarossi:** Writing – review & editing, Writing – original draft, Validation, Methodology, Investigation, Conceptualization. **Yassmine Rghif:** Writing – review & editing, Writing – original draft, Validation, Software, Methodology, Conceptualization.

## Declaration of competing interest

The authors declare that they have no known competing financial interests or personal relationships that could have appeared to influence the work reported in this paper.

## Data availability

Data will be made available on request.

## References


[1] A. Kasaeian, S. Sharifi, W.M. Yan, Novel achievements in the development of solar ponds: a review, Sol. Energy 174 (2018) 189–206, https://doi.org/10.1016/j.solener.2018.09.010. June.

[2] M. Khalilian, H. Pourmokhtar, A. Roshan, Effect of heat extraction mode on the overall energy and exergy efficiencies of the solar ponds: a transient study, Energy 154 (2018) 27–37, https://doi.org/10.1016/j.energy.2018.04.120.

[3] A. Nait Brahim, Y. Rghif, F. Bahraoui, Numerical investigation of solar energy storage by a salt gradient solar pond in several Moroccan cities, E3S Web Conf. 20 (2022), https://doi.org/10.1051/e3sconf/202233600020.

[4] M. Mazidi, M.H. Shojaeefard, M.S. Mazidi, H. Shojaeefard, Two-dimensional modeling of a salt-gradient solar pond with wall shading effect and thermo-physical properties dependent on temperature and concentration, J. Therm. Sci. 20 (4) (2011) 362–370, https://doi.org/10.1007/s11630-011-0482-5.

[5] Y. Rghif, B. Zeghmati, F. Bahraoui, Numerical study of Soret and Dufour coefficients on heat and mass transfer in a salt gradient solar pond, AIP Conf. Proc. (April, 2021) 020003, https://doi.org/10.1063/5.0049389.

[6] Y. Rghif, B. Zeghmati, F. Bahraoui, Soret and Dufour effects on thermal storage and storage efficiency of a salt gradient solar pond, IEEE Xplore 5 (2020), https://doi.org/10.1109/REDEC49234.2020.9163880.

[7] Y. Rghif, D. Colarossi, P. Principi, Salt gradient solar pond as a thermal energy storage system: a review from current gaps to future prospects, J. Energy Storage 61 (2023) 106776, https://doi.org/10.1016/j.est.2023.106776.

[8] K. Nakoa, K. Rahaoui, A. Date, A. Akbarzadeh, An experimental review on coupling of solar pond with membrane distillation, Sol. Energy 119 (2015) 319–331, https://doi.org/10.1016/j.solener.2015.06.010.

[9] K. Manzoor, S.J. Khan, Y. Jamal, M.A. Shahzad, Heat extraction and brine management from salinity gradient solar pond and membrane distillation, Chem. Eng. Res. Des. 118 (2017) 226–237, https://doi.org/10.1016/j.cherd.2016.12.017.

[10] B.M. Ziapour, M. Saadat, V. Palideh, S. Afzal, Power generation enhancement in a salinity-gradient solar pond power plant using thermoelectric generator, Energy Convers. Manag. 136 (2017) 283–293, https://doi.org/10.1016/j.enconman.2017.01.031.

[11] Y. Rghif, B. Zeghmati, F. Bahraoui, Soret and Dufour effects on thermosolutal convection developed in a salt gradient solar pond, Int. J. Therm. Sci. 161 (November 2020) 106760, https://doi.org/10.1016/j.ijthermalsci.2020.106760, 2021.

[12] Y. Rghif, B. Zeghmati, F. Bahraoui, Numerical analysis of the influence of buoyancy ratio and Dufour parameter on thermosolutal convection in a square salt gradient solar pond, Fluid Dyn. Mater. Process. (2022), https://doi.org/10.32604/fdmp.2022.021500.

[13] M.R. Assari, H. Basirat Tabrizi, M. Parvar, A. Kavoosi Nejad, A. Jafar Gholi Beik, Experiment and optimization of mixed medium effect on small-scale salt gradient solar pond, Sol. Energy 151 (2017) 102–109, https://doi.org/10.1016/j.solener.2017.04.042.

[14] H. Wang, X. Yu, F. Shen, L. Zhang, A Laboratory experimental study on effect of porous medium on salt diffusion of salt gradient solar pond, Sol. Energy 122 (2015) 630–639, https://doi.org/10.1016/j.solener.2015.09.005.

[15] Y. Rghif, A. Sayer, H.B. Mahood, Transient behavior of a salinity gradient solar pond under Mediterranean climate, J. Sol. Energy Eng. 145 (October) (2023) 1–33, https://doi.org/10.1115/1.4056788.

[16] M. Husain, G. Sharma, S.K. Samdarshi, Innovative design of non-convective zone of salt gradient solar pond for optimum thermal performance and stability, Appl. Energy 93 (2012) 357–363, https://doi.org/10.1016/j.apenergy.2011.12.042.

[17] M. Husain, P.S. Patil, S.R. Patil, S.K. Samdarshi, Optimum size of non-convective zone for improved thermal performance of salt gradient solar pond, Sol. Energy 74 (5) (2003) 429–436, https://doi.org/10.1016/S0038-092X(03)00157-9.

[18] J.A. Ruskowitz, F. Suárez, S.W. Tyler, A.E. Childress, Evaporation suppression and solar energy collection in a salt-gradient solar pond, Sol. Energy 99 (2014) 36–46, https://doi.org/10.1016/j.solener.2013.10.035.

[19] J.F. Atkinson, D.R.F. Harleman, A wind-mixed layer model for solar ponds, Sol. Energy 31 (3) (1983) 243–259, https://doi.org/10.1016/0038-092X(83)90012-9.

[20] Y. Rghif, B. Zeghmati, F. Bahraoui, Modeling of a salt gradient solar pond under Moroccan climate taking into account double-diffusive convection, Mater. Today Proc. 30 (2020) 883–888, https://doi.org/10.1016/j.matpr.2020.04.345.

[21] S. Prajapati, N. Mehta, S. Yadav, An overview of factors affecting salt gradient solar ponds, Mater. Today Proc. 56 (2022) 2742–2752, https://doi.org/10.1016/j.matpr.2021.09.538.

[22] A. El Mansouri, M. Hasnaoui, A. Amahmid, R. Bennacer, Transient modeling of a salt gradient solar pond using a hybrid Finite-Volume and Cascaded Lattice-Boltzmann method: thermal characteristics and stability analysis, Energy Convers. Manag. 158 (2018) 416–429, https://doi.org/10.1016/j.enconman.2017.12.085. January.

[23] Y. Rghif, D. Colarossi, P. Principi, Effects of double-diffusive convection on calculation time and accuracy results of a salt gradient solar pond: numerical investigation and experimental validation, Sustainability 15 (2) (2023) 1479, https://doi.org/10.3390/su15021479.

[24] J. Pereira da Cunha, P. Eames, Thermal energy storage for low and medium temperature applications using phase change materials - a review, Appl. Energy 177 (2016) 227–238, https://doi.org/10.1016/j.apenergy.2016.05.097.

[25] N. Zhang, Y. Yuan, X. Cao, Y. Du, Z. Zhang, Y. Gui, Latent heat thermal energy storage systems with solid–liquid phase change materials: a review, Adv. Eng. Mater. 20 (6) (2018) 2023, https://doi.org/10.1002/adem.201700753.

[26] M.R. Assari, H. Basirat Tabrizi, A. Jafar Gholi Beik, Experimental studies on the effect of using phase change material in salinity-gradient solar pond, Sol. Energy 122 (2015) 204–214, https://doi.org/10.1016/j.solener.2015.07.053.

[27] M. Ines, P. Paolo, F. Roberto, S. Mohamed, Experimental studies on the effect of using phase change material in a salinity-gradient solar pond under a solar simulator, Sol. Energy 186 (April) (2019) 335–346, https://doi.org/10.1016/j.solener.2019.05.011.

[28] J.A.G. Beik, M.R. Assari, H. Basirat Tabrizi, Transient modeling for the prediction of the temperature distribution with phase change material in a salt-gradient solar pond and comparison with experimental data, J. Energy Storage 26 (September) (2019) 101011, https://doi.org/10.1016/j.est.2019.101011.

[29] Y. Rghif, B. Zeghmati, F. Bahraoui, Modeling the influences of a phase change material and the Dufour effect on thermal performance of a salt gradient solar pond, Int. J. Therm. Sci. 166 (2021) 106979, https://doi.org/10.1016/j.ijthermalsci.2021.106979. March.

[30] D. Colarossi, P. Principi, Experimental investigation and optical visualization of a salt gradient solar pond integrated with PCM, Sol. Energy Mater. Sol. Cells 234 (2022), https://doi.org/10.1016/j.solmat.2021.111425.

[31] M.R. Assari, A. Jafar Gholi Beik, R. Eydi, H. Basirat Tabrizi, Thermal-salinity performance and stability analysis of the pilot salt-gradient solar ponds with phase change material, Sustain. Energy Technol. Assessments 53 (2022) 102396, https://doi.org/10.1016/j.seta.2022.102396.

[32] I. Al-Iessa, R. Maddahian, M. Maerefat, Investigation of the PCM layer thickness and heat extraction on the thermal efficiency of salt gradient solar ponds, Case Stud. Therm. Eng. 45 (2023) 103014, https://doi.org/10.1016/j.csite.2023.103014.

[33] D. Colarossi, M. Pezzuto, P. Principi, Effect of PCM melting temperature on solar ponds performance: design and experimental investigation, Sol. Energy 242 (2022) 225–233.

[34] M. Arulprakasajothi, N. Poyyamozhi, P. Chandrakumar, N. Dilip Raja, D. Yuvarajan, Experimental investigation of salinity gradient solar pond with nano-based phase change materials, Energy Sources, Part A Recover. Util. Environ. Eff. 45 (2) (2023) 5465–5480, https://doi.org/10.1080/15567036.2023.2207508.

[35] R. Boudhiaf, M. Baccar, Transient hydrodynamic, heat and mass transfer in a salinity gradient solar pond: a numerical study, Energy Convers. Manag. 79 (2014) 568–580, https://doi.org/10.1016/j.enconman.2013.12.068.

[36] H.C. Bryantt, I.A.N. Colbeck, A solar pond for London? Sol. Energy 19 (1977) 321–322.

[37] Y. Rghif, F. Bahraoui, B. Zeghmati, Experimental and numerical investigations of heat and mass transfer in a salt gradient solar pond under a solar simulator, Sol. Energy 236 (2022) 841–859, https://doi.org/10.1016/j.solener.2022.03.033. February.

[38] A. Sharma, V. V Tyagi, C.R. Chen, D. Buddhi, Review on thermal energy storage with phase change materials and applications, Renew. Sustain. Energy Rev. 13 (2009) 318–345, https://doi.org/10.1016/j.rser.2007.10.005.

[39] Rubitherm, Organic PCM, 2024. https://www.rubitherm.eu/en/productcategory/organische-pcm-rt.

[40] S.V. Patankar, Numerical Heat Transfer and Fluid Flow, 1980.

[41] D. Colarossi, E. Tagliolini, P. Principi, R. Fioretti, Design and validation of an adjustable large-scale solar simulator, Appl. Sci. 11 (4) (2021), https://doi.org/10.3390/app11041964.